Short Papers

A Three-Dimensional Magnetic Tweezer System for Intraembryonic Navigation and Measurement

Xian Wang, Mengxi Luo, Han Wu, Zhuoran Zhang, Jun Liu, Zhensong Xu, Wesley Johnson, and Yu Sun

***Abstract*—Magnetic micromanipulation has the advantage of untethered control, high precision, and biocompatibility and has recently undergone great advances. The magnetic micromanipulation task to tackle in this paper is to three dimensionally navigate a 5-μm magnetic bead inside a mouse embryo and accurately apply forces to intraembryonic structures to perform mechanical measurements at multiple locations. Existing technologies are not able to achieve these navigation and measurement goals because of poor magnetic force scaling and/or lacking the capability of applying an accurately controlled force. This paper reports a three-dimensional magnetic tweezer system that enables, for the first time, intraembryonic magnetic navigation and force application. A single magnetic bead was introduced into a mouse embryo via robotic microinjection. The magnetic tweezer system accurately controlled the position of the magnetic bead via visually servoed magnetic control. By moving the magnetic bead with known forces inside the embryo, cytoplasm viscosity was measured, which is eight times the viscosity of water. For performing mechanical measurements on the cellular structures inside the mouse embryo, the system should be capable of applying forces up to 120 pN with a resolution of 4 pN. The results revealed that the middle region is significantly more deformable than the side regions of the inner cell mass.**

***Index Terms*—Cell manipulation, intraembryonic measurement, magnetic micromanipulation, micro-/nanorobotics.**

I. Introduction

Recent studies have shown that mechanical inputs play a major role in regulating cell fate during early mammalian embryo development, yet little is known about the biomechanical properties of the intraembryonic environment and intraembryonic structures [1]–[4]. The ICM of the embryo undergoes compaction and shape changes, eventually giving rise to the definitive structures of the fetus [5]. However, the intraembryonic viscosity and the biomechanical properties of the ICM in early-stage embryos is largely unknown because of the lack of a suitable intraembryonic measurement technique [6], [7].

To measure mechanical properties inside an embryo, a micrometer-sized tool is required, which must be positioned accurately along the three dimensions and be capable of applying well-controlled forces to the cellular structures (see Fig. 1). Due to the thick outer membrane surrounding the embryo (i.e., zona pellucida or ZP), traditional contact-based techniques are not able to perform intraembryonic measurement. For instance, atomic force microscopy (AFM) cantilevers and the blunt micropipette tips for micropipette aspiration cannot penetrate the embryo and reach the ICM [8], [9]. We previously used a sharp micropipette tip to penetrate ZP of a mouse embryo and applied a high-speed fluidic jet to deform the intraembryonic structures for mechanical measurements [10]. However, the motion of the tethered micropipette tip after ZP penetration was severely constrained, limiting its accurate positioning inside the embryo for multilocation measurements. Laser trapping is capable of untethered manipulation and measurement [11]; however, it typically has a low force output (e.g., 10 pN), which is insufficient to deform inner embryonic structures.

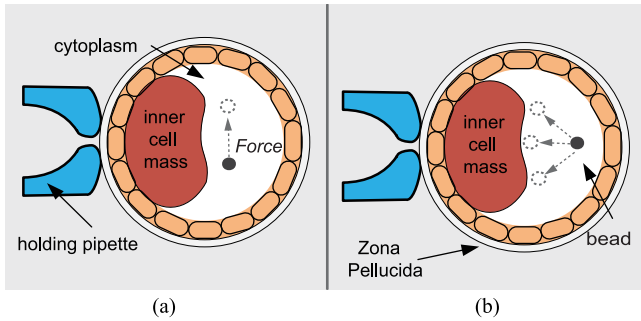

Fig. 1. Intraembryonic navigation and mechanical measurement inside a mouse embryo. (a) Schematic of measuring intraembryonic viscosity through navigating the magnetic controlled microbead inside the embryo with a known force. (b) Schematic of mechanical characterization of multiple locations on the inner cell mass (ICM) of the mouse embryo.

Recently, three-dimensional (3-D) magnetic micromanipulation has undergone significant advances, leveraging torque-generated or gradient-generated forces [12]. Generating forces by torque requires a helical tail of more than 100 μm for exerting tens of picoNewton forces, unsuitable for measurement inside a cell (e.g., 20 μm) [13]–[15]. Gradient pulling forces can be generated by several magnetic field configurations [16]–[19]. However, existing techniques are not able to efficiently three dimensionally control an object below 10 μm due to poor magnetic force scaling or lacking the capability of applying an accurately controlled force. Conventional magnetic tweezers can generate large forces (e.g., hundreds of picoNewton) [20], [21]; however, the single-axis actuation nature makes it incapable of positioning a magnetic bead arbitrarily in a 3-D workspace.

Table I summarizes five representative 3-D magnetic micromanipulation methods. Besides the advantages and limitations shown in the table, it should be understood that when a 5-μm magnetic bead (gravity: $\sim$10 pN) is placed on these setups, it is likely that none of the

Manuscript received August 16, 2017; accepted October 9, 2017. Date of publication November 21, 2017; date of current version February 5, 2018. This paper was recommended for publication by Associate Editor C. Bergeles and Editor P. Dupont upon evaluation of the reviewers' comments. This work was supported by the Natural Sciences and Engineering Research Council of Canada under a Discovery Grant and in part by the Canada Research Chairs Program. *(Corresponding author: Yu Sun.)*

The authors are with the Department of Mechanical and Industrial Engineering, University of Toronto, Toronto, ON M5S 3G8, Canada (e-mail: wangxiantju@hotmail.com; bonnie.luo@mail.utoronto.ca; sswuhan@outlook.com; zhuoran@mie.utoronto.ca; ljun@mie.utoronto.ca; Zhensong.xu@mail.utoronto.ca; wes.johnson@mail.utoronto.ca; sun@mie.utoronto.ca).

This paper has supplementary downloadable material available at http://ieeexplore.ieee.org.

Color versions of one or more of the figures in this paper are available online at http://ieeexplore.ieee.org.

Digital Object Identifier 10.1109/TRO.2017.2765673

TABLE I
REPRESENTATIVE 3-D MAGNETIC MICROMANIPULATION SYSTEMS

Method	Helmholtz coils (for Helical swimmer) [13]–[15]	Rotating permanent magnets setup [18]	MiniMag [16], [17]	MRI-based platform [19]	Hexapole magnetic tweezers [22], [23]
Actuation method	Force generated by rotatory magnetic torque	Gradient-generated force by permanent magnets	Gradient-generated force by eight-coil setup	Gradient-generated force by MRI coils	Gradient-generated force near sharp tips
Actuation field	$B = 2$ mT, $f = 30$ Hz	$\nabla B_{\max} = 0.9$ T/m	$\nabla B_{\max} = 5$ T/m	$\nabla B_{\max} = 0.45$ T/m	$\nabla B_{\max} = 50$ T/m
Dimensions of magnetic object/robot	Tail length: 50 μm [14], [15], 8.8 μm [14]	250-μm cubic magnet	500 μm $\times$ 250 μm $\times$ 70 μm; 0.2 μm $\times$ 10 μm nanowire; 5- μm-diameter microbead	1.5 mm-diameter bead	4.5 μm-diameter microbead
Advantages	Torque-based force scales by a power of two with the dimension reduction of the object, while gradient pulling scales by a power of three.	Low heat generation compared to electromagnets; multiple locomotion methods (e.g., rotating, gradient pulling, and stick-slip)	Multiple locomotion methods (e.g., rotating, gradient pulling, and stick-slip)	Availability of simultaneous deep-body image feedback; no additional setup required	High gradient field produced at the sharp tips
Limitations	A long tail is needed to generate sufficient propulsion forces. Step-out frequency limits propulsive force increase even with the increase of rotation frequency.	Low-frequency field modulation; field cannot be turned OFF.	Field is limited by the size, resistance, and heat generation of coil wires.	High cost; small magnetic field gradient that decays by a power of four in the large MRI workspace.	Misalignment of poles can cause unbalanced forces.
Max force on a 5-μm bead	3 pN with a tail of 50 μm in length [15]	2 pN	10 pN	1 pN	100 pN

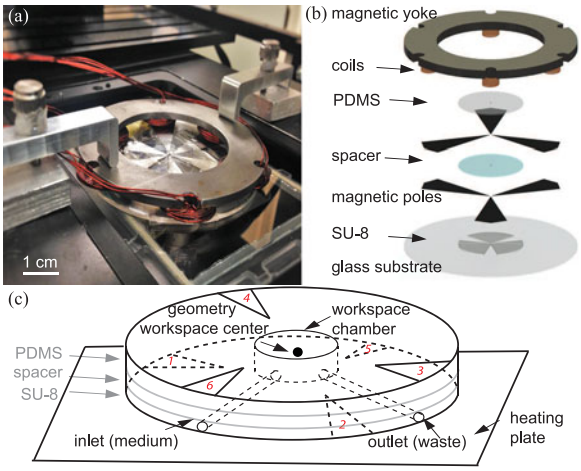

Fig. 2. (a) 3-D magnetic tweezer system. (b) Different layers and structures of the magnetic tweezers. (c) The bottom layer poles are labeled with number 1, 2, and 5, and the top layer poles are labeled with number 3, 4, and 6. Cell culture medium exchange is through the inlet and outlet ports.

techniques except the hexapole magnetic tweezers (see Fig. 2) are able to produce sufficient forces to levitate the bead. The hexapole magnetic tweezers use sharp tips and a small workspace to compensate for the scaling of magnetic moment and gradient decay, providing sufficient forces to balance gravity and thermal fluctuations.

This paper presents a new hexapole magnetic tweezer system to enable intraembryonic navigation and measurement. The 3-D magnetic manipulation system has the following unique capabilities:

1) an integrated design that maintains cells inside a temperature and culture medium controlled environment;
2) accurate positioning of a 5-μm magnetic bead three dimensionally;
3) accurate application of forces that are quantified through the development of a new force model relating force with driving current and bead locations;
4) manipulation force experimentally calibrated by deforming an AFM cantilever.

The 3-D magnetic tweezer performed mechanical measurements inside individual mouse embryos. The viscosity measurements revealed that the cytoplasm viscosity is about eight times the viscosity of water, and the force–displacement data provided direct evidence of the inhomogeneous mechanical properties of the ICM.

II. SYSTEM DESIGN

The 3-D magnetic tweezer system, as shown in Fig. 2, consists of six magnetic poles with sharp tips (three poles placed in one plane and the other three poles placed in a different plane), a magnetic yoke, and coils. To achieve a large magnetic field gradient, the magnetic poles were made of high permeability foils (shielding alloys, MuShield) and the tips were fabricated by electrical discharge machining. The magnetic yoke strengthens the magnetic field by connecting all poles into a complete magnetic circuit. Coils were wired onto the cores on the yoke. The magnetic poles were embedded in polydimethylsiloxane (PDMS) to protect ferromagnetic beads from attaching to the poles, which would create unbalanced magnetic pole pairs. Fluid inlet and outlet channels of the system were fabricated in the PDMS structure, enabling cell culture medium exchange in and out of the workspace chamber. Key design parameters are summarized in Table II.

In fabrication, SU-8 photolithography was conducted on a glass substrate to form the shape of the workspace chamber, the inlet and outlet, and alignment marks. Then, a PDMS membrane (200 μm in

TABLE II
KEY PARAMETERS IN SYSTEM DESIGN

Symbol	Description	Value	Effects
D	Distance from pole tip to workspace center	400 μm	Magnetic field gradient
$I_{\max}$	Maximum current values	$\pm$2 A	Magnetic force magnitude
n	Number of turns in each coil	40	Magnetic force resolution, magnetic force magnitude
d	Magnetic bead diameter	4.0–4.9 μm	Magnetic force, thermal fluctuation

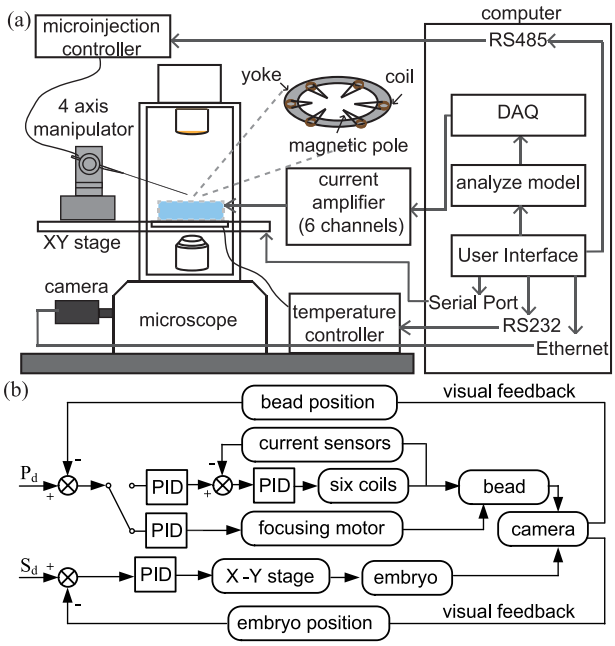

Fig. 3. (a) 3-D magnetic tweezer system setup. (b) Control architecture of the 3-D magnetic tweezer system for controlling a single 5-μm magnetic bead for 3-D positioning and measurement. The microbead target position P_d is under global image coordinates. The stage target position S_d is under global 3-D coordinates.

thickness) with a hole in the center was aligned onto the SU-8 layer to cover the inlet and outlet channels. The three bottom layer magnetic poles were mounted onto the substrate using the alignment marks fabricated on SU-8. A 300-μm-thick spacer with a hole in the center was assembled onto the top of the three poles, ensuring that the hole was aligned with the workspace chamber. The three top layer poles were then assembled onto the spacer following additional alignment marks. Finally, PDMS was poured onto the assembly around the spacer to cover the poles, leaving only the workspace chamber accessible.

The magnetic tweezer device was placed on a standard inverted microscope (Nikon TE2000-S) with a motorized *XY* translation stage (ProScan, Prior Scientific, Inc.), a temperature controlled heating plate (microplate heater, Cell MicroControls), and a four-axis micromanipulator (MX7600, Siskiyou, Inc.) that controls micropipette positioning for microinjection of a ferromagnetic bead (CFM-40-10, Spherotech, diameter: 4.0–4.9 μm, permeability: 0.35 H/m) into the embryos [see Fig. 3(a)]. The bead position in the XY plane is visually detected by microscopy imaging and visual tracking. The bead's *Z* position is controlled via computing focus measures and motorized focus adjustment. The system's control architecture is summarized in Fig. 3(b), where P_d is the target position for microbead position control and S_d is the target position for the motorized stage to move the magnetic workspace to the center of the field of view.

The experimental process consists of two stages, including magnetic bead microinjection and intraembryonic navigation/measurement. A single magnetic bead was injected into a mouse embryo via robotic microinjection [10], which relies on vision and position feedback to cooperatively control the robotic micromanipulator and *XY* stage. A single ferromagnetic bead was picked up by micropipette aspiration and injected into the embryo using a sharp micropipette with an inner diameter of 5 μm. The system visually detects the embryo and coordinates the *XY* stage to move the magnetic workspace into the center of the field of view. The bead position was controlled three dimensionally by regulating current in the coils and using visual feedback for visual servo control. Magnetic force exerted on the bead was also controlled by adjusting current in the coils. Besides visual tracking of bead positions in plane, focus–defocus was used to estimate and track the *Z* positions of the bead at 30 Hz.

TABLE III
NOTATIONS IN FORCE MODELING

Symbol	Description
q_j	Magnetic charge representing pole j
r_j	Distance from a position in workspace to the magnetic charge
$\boldsymbol{u_j}$	Unit vector from a position toward the magnetic charge
l	Effective distance from magnetic charge to the workspace center

III. MODELING OF MULTIPOLE MAGNETIC TWEEZERS

Within the workspace, the ferromagnetic microbead is magnetized by the magnetic field that is generated when current is supplied to the coils. Zhang *et al.* developed a magnetic field model relating the normalized force and the normalized current [24]. This normalized model enables 3-D position control, but does not describe force quantification. As force information is necessary for mechanical characterization, we present a force model to relate the force exerted on the microbead, current, and microbead position (with notations summarized in Table III). The microbead dynamics is then analyzed. With the developed magnetic force model, the magnetic force can be precisely quantified for mechanical measurements.

A. Magnetic Force Modeling

According to the Gauss law of magnetism, each magnetic pole with a sharp tip can be represented by a magnetic charge, q [24], for simplicity. Based on superposition, the magnetic field generated by six magnetic charges is

$$\boldsymbol{B} = \sum_{j=1}^{6} \frac{\mu_0 q_j}{4\pi r_j^2} \boldsymbol{u_j} = \sum_{j=1}^{6} \frac{k_m q_j}{r_j^2} \boldsymbol{u_j} \tag{1}$$

where μ_0 is the permeability of vacuum, $k_m = \mu_0/4\pi$, r_j, and $\boldsymbol{u_j}$ represent the distance from a position in the workspace to the magnetic charge and the unit vector in that direction, respectively. The ferromagnetic microbead is magnetized by the field, and the magnetic moment before saturation is

$$\boldsymbol{m_b} = \frac{3V}{\mu_0} \left(\frac{\mu - \mu_0}{\mu + 2\mu_0} \right) \boldsymbol{B} \tag{2}$$

where μ is the permeability of the microbead, and V is the microbead's volume. The induced magnetic moment $\boldsymbol{m_b}$ always aligns itself with the applied field $\boldsymbol{B}$ since there is no shape anisotropy for the spherical microbead. This simplifies the model as the bead is subjected to pure force and zero magnetic torque.

The relationship between force and magnetic charge q is

$$\begin{aligned}\boldsymbol{F} &= \nabla\left(\frac{1}{2}\boldsymbol{m_b}\cdot\boldsymbol{B}\right)\\ &= \frac{3V}{2\mu_0}\left(\frac{\mu-\mu_0}{\mu+2\mu_0}\right)\frac{k_m^2}{l^4}\sum_{j=1}^{6}q_j\sum_{k=1}^{6}q_k\nabla\left(\frac{\boldsymbol{u_j}\cdot\boldsymbol{u_k}}{\hat{r}_j^2\hat{r}_k^2}\right)\end{aligned} \tag{3}$$

where l is the distance from the effective workspace center to the position of magnetic charge, and $\hat{r}_j = r_j/l$, $\hat{r}_k = r_k/l$.

Let $k_q = 3V(\mu-\mu_0)k_m^2/2\mu_0 l^4(\mu+2\mu_0)$. $\boldsymbol{M}$ is a six-by-six matrix, and $\boldsymbol{M}(j,k) = (\boldsymbol{u_j}\cdot\boldsymbol{u_k}/\hat{r}_j^2\hat{r}_k^2)$. The vector $\boldsymbol{Q} = [q_1, q_2, q_3, q_4, q_5, q_6]^T$ represents all magnetic charges. Then, (3) can be simplified to

$$\boldsymbol{F} = k_q\nabla(\boldsymbol{Q}^T\boldsymbol{M}\boldsymbol{Q}) \tag{4}$$

From the magnetic circuit analysis in [24], the magnetic charge value depends on the current in the coil, namely

$$\boldsymbol{Q} = \frac{\boldsymbol{\Phi}}{\mu_0} = \frac{n}{\mu_0 R_{\mathrm{mag}}}\boldsymbol{K_I}\boldsymbol{I} \tag{5}$$

where $\boldsymbol{\Phi}$ is the matrix of magnetic flux that is produced by each magnetic charge, n represents the number of turns in each coils, R_{mag} is the magnetic reluctance, determined by the magnetic properties of the poles, yoke, and medium, and $\boldsymbol{K_I}$ is the distribution matrix of magnetic flux, derived from [24].

By relating magnetic charge $\boldsymbol{Q}$ to electric current $\boldsymbol{I}$, the magnetic force can be rewritten as

$$\boldsymbol{F} = k_q\left(\frac{n}{\mu_0 R_{\mathrm{mag}}}\right)^2\nabla[\boldsymbol{I}^T(\boldsymbol{K_I}^T\boldsymbol{M}\boldsymbol{K_I})\boldsymbol{I}] = k_i\nabla(\boldsymbol{I}^T\boldsymbol{N}\boldsymbol{I}) \tag{6}$$

where $\boldsymbol{N} = \boldsymbol{K_I}^T\boldsymbol{M}\boldsymbol{K_I}$. The coefficient k_i relates current and force, and $k_i = k_q(n/\mu_0 R_{\mathrm{mag}})^2$.

As no net magnetic charge exists, the summation of all magnetic charge is zero. Thus, the constraint condition is set on the driving current, $\sum_{j=1}^{6} I_j = 0$. Then, the magnetic force of three directions in the effective workspace center can be expressed by the current values in each coil. Suppose the magnetic microbead is located at the effective workspace center, the magnetic force acted on the microbead is

$$\boldsymbol{F_c} = k_i\nabla(\boldsymbol{I}^T\boldsymbol{N_0}\boldsymbol{I}) \tag{7}$$

where $\boldsymbol{N_0} = \boldsymbol{N}|_{x=y=z=0} = \boldsymbol{K_I}^T\boldsymbol{M}|_{r=l}\boldsymbol{K_I}$.

Based on $\boldsymbol{F_c}$, the magnetic force at other locations in the workspace can be calculated through Taylor series expansion of the magnetic field calculation. According to [22]–[24], force calculation is simplified by the first order of Taylor series expansion. The normalized force is expressed as

$$(\hat{F}_x, \hat{F}_y, \hat{F}_z) = \left(\hat{F}_{cx} + \frac{8x}{l}, \hat{F}_{cy} + \frac{8y}{l}, \hat{F}_{cz} + \frac{32z}{l}\right) \tag{8}$$

where $(\hat{F}_x, \hat{F}_y, \hat{F}_z)$ is the normalized magnetic force in the three dimensions, $(\hat{F}_{cx}, \hat{F}_{cy}, \hat{F}_{cz})$ is the normalized values of the center force $\boldsymbol{F_c}$ described in (7), and (x, y, z) is the location of the magnetic microbead.

Substituting (7) into (8) gives

$$\begin{aligned}\boldsymbol{F} &= \boldsymbol{F_c} + k_i {I_{\max}}^2\begin{bmatrix}\frac{8}{l} & 0 & 0\\ 0 & \frac{8}{l} & 0\\ 0 & 0 & \frac{32}{l}\end{bmatrix}\begin{bmatrix}x\\ y\\ z\end{bmatrix}\\ &= k_i {I_{\max}}^2\nabla(\hat{\boldsymbol{I}}^{\boldsymbol{T}}\boldsymbol{N_0}\hat{\boldsymbol{I}}) + k_i {I_{\max}}^2\boldsymbol{K}\boldsymbol{P}\end{aligned} \tag{9}$$

where $I_{\max}$ is the maximum current in each coil, $\hat{\boldsymbol{I}} = \boldsymbol{I}/I_{\max}$ is the normalized current, and $\boldsymbol{P}$ is the bead position in the workspace. The matrix $\boldsymbol{K}$ is calculated from the first order of Taylor series expansion. The values of k_i and l are experimentally calibrated.

B. Microbead Dynamics and Controller Design

The microbead is subjected to magnetic force, drag force, thermal fluctuations, buoyancy, and gravity in the workspace. Thermal disturbance can be modeled as white noise, which depends on temperature and the size of the microbead. Then, the momentum change of the microbead $m\Delta\boldsymbol{v}$ is

$$(\boldsymbol{F} - 6\pi\eta r\boldsymbol{v} + \boldsymbol{F_b} - \boldsymbol{G})\Delta t = m\Delta\boldsymbol{v} \tag{10}$$

where $\boldsymbol{F}$ represents the magnetic force, η is the viscosity of the medium, $\boldsymbol{v}$ is the speed of the microbead, $6\pi\eta r\boldsymbol{v}$ is the fluid drag force, $\boldsymbol{F_b}$ is the buoyant force, and $\boldsymbol{G}$ is the gravity. Substituting (9) into (10) gives

$$[k_i\nabla(\boldsymbol{I}^{\boldsymbol{T}}\boldsymbol{N_0}\boldsymbol{I}) + k_i {I_{\max}}^2\boldsymbol{K}\boldsymbol{P} - 6\pi\eta r\boldsymbol{v} + \rho g V - \boldsymbol{G}]\Delta t = m\Delta\boldsymbol{v}. \tag{11}$$

For bead position control, the bead position in the Z-direction is detected through focus–defocus, and the bead is levitated through controlling currents I_5 and I_6. In the meanwhile, the bead position in XY is visually detected and set as input of the controller for calculating currents I_1, I_2, I_3, I_4. Since the summation of currents in each pair of coils is constant, the current matrix is

$$\boldsymbol{I} = \begin{bmatrix}I_1\\ I_2\\ I_3\\ I_4\\ I_5\\ I_6\end{bmatrix} = \begin{bmatrix}I_{\max}/2 + \Delta I_1\\ -I_{\max}/2 + \Delta I_2\\ I_{\max}/2 - \Delta I_1\\ -I_{\max}/2 - \Delta I_2\\ I_5\\ I_6\end{bmatrix} \tag{12}$$

where ΔI_1 and ΔI_2 are the controller output.

Based on the microbead dynamics from (11) and (12), the transfer function of the system is

$$G(s) = [s\boldsymbol{U}_{2X2} - \boldsymbol{A}]^{-1}\boldsymbol{B} \tag{13}$$

where $\boldsymbol{U}_{2X2} = \left[\begin{smallmatrix}1 & 0\\ 0 & 1\end{smallmatrix}\right]$, $\boldsymbol{A} = \frac{k_i {I_{\max}}^2\boldsymbol{K}}{6\pi\eta r\boldsymbol{v} + m/t}$, and $\boldsymbol{B} = \frac{k_i}{6\pi\eta r\boldsymbol{v} + m/t}\left[\begin{smallmatrix}\Delta I_1\\ \Delta I_2\end{smallmatrix}\right]$. Then, the PID controller is,

$$\begin{bmatrix}\Delta I_1\\ \Delta I_2\end{bmatrix} = K_p\boldsymbol{E} + K_i\int\boldsymbol{E}dt + K_D\frac{d\boldsymbol{E}}{dt} \tag{14}$$

where $\boldsymbol{E} = \boldsymbol{P}_{\mathrm{set}} - \boldsymbol{P}$. The initial values of the controller gain K_p, K_i, K_d were set by simulations (13) and further tuned in experiments.

C. Magnetic Field Simulation

To validate the force model shown in (9), magnetic field simulation was conducted in ANSYS Maxwell to determine the effective workspace area and the relationship between force, bead position, and maximum current.

As the analysis of magnetic field distribution along the X, Y, Z directions is the same, only the force and position in the $+X$-direction was simulated. In simulation, the magnetic field was first generated and

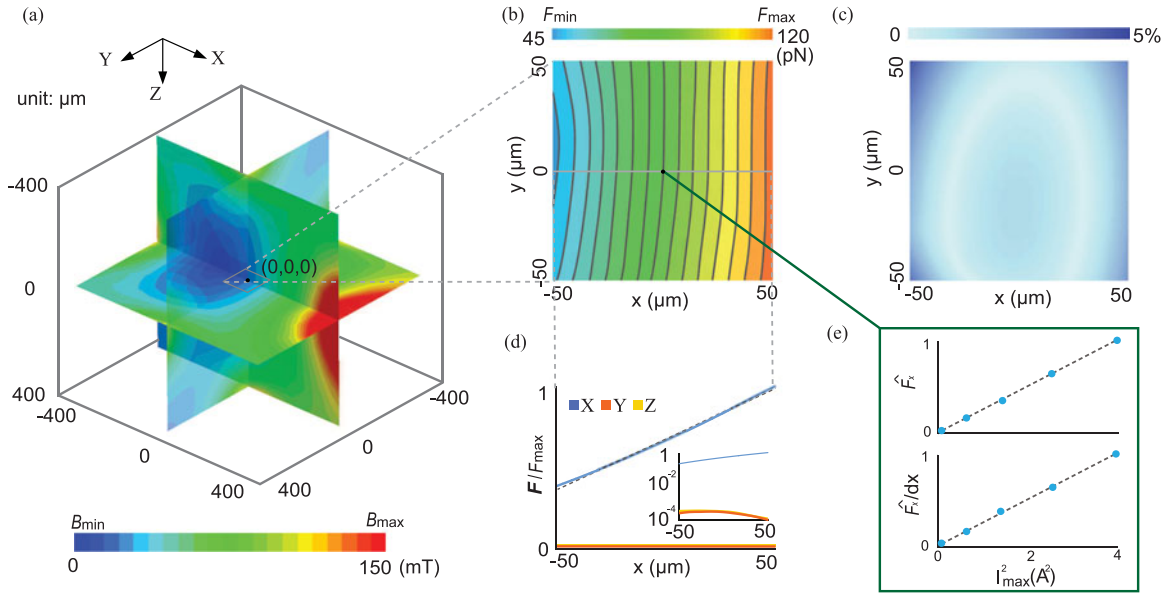

Fig. 4. Magnetic field simulation for model validation. (a) Simulated magnetic field and force generation in the $+X$-direction. Current values applied to each coil (coils and poles not shown) are 2, -0.67, -0.67, 0.67, -0.67, and -0.67 A. The current values were selected with the target of generating a force of 80 pN in the workspace center. In simulation, the workspace center was chosen as the coordinate origin of the global coordinate system. (b) Simulated force field for a 5-μm pure iron bead in the workspace of 100 μm $\times$ 100 μm in the XY plane. The maximum force within the workspace is 120 pN. (c) Force error map in the area of 100 μm $\times$ 100 μm in the XY plane. The error is defined as the difference between the simulation results and the model calculated values. (d) Relationship between normalized force $\hat{F_x}$ and the bead position in the X-axis. In this case, forces along Y and Z are less than 1% of the force along X. (e) Relationship between normalized force in the $+X$-direction, the gradient of force, and the square of maximum current value.

maintained constant by applying constant current to each coil for generating a field gradient only in the $+X$-direction in the workspace center [see Fig. 4(a)], with pole positions not shown. For a 5-μm iron bead within the field, the force on the bead was estimated through the law of magnetization. Fig. 4(b) shows force distribution in the XY plane, where the colors represent force magnitudes. The simulation results proved that the generated force is linearly dependent on the position of the bead within an area of 100 μm $\times$ 100 μm $\times$ 100 μm around the workspace center. In addition, the error of magnetic force between simulated results and model calculated results was also quantified [see Fig. 4(c)], which is less than 5% throughout the workspace of 100 μm $\times$ 100 μm $\times$ 100 μm.

After the relationship between force and bead position was studied with a constant current applied to each coil, bead position was set to be the workspace center and current values were varied to validate the relationship between force and current. In simulation, $I_{\max}$ was varied to quantify the generated forces under different magnitudes of the driving current. As summarized in Fig. 4(e), the force on the magnetic bead that was placed at the workspace center (i.e., constant bead position) increases linearly with the square of maximum current $I_{\max}$. This validates the quadratic relationship between current magnitude and force in (9).

The magnetic field simulations proved the linear relationship between force and bead position, and the quadratic relationship between force and driving current. However, the values of k_i and l need to be calibrated experimentally.

IV. Experiments and Discussion

A. System Calibration

Equation (9) reveals that magnetic force depends on driving currents and the position of the microbead in the workspace. Due to the imperfect alignment of the poles in fabrication, the effective workspace center

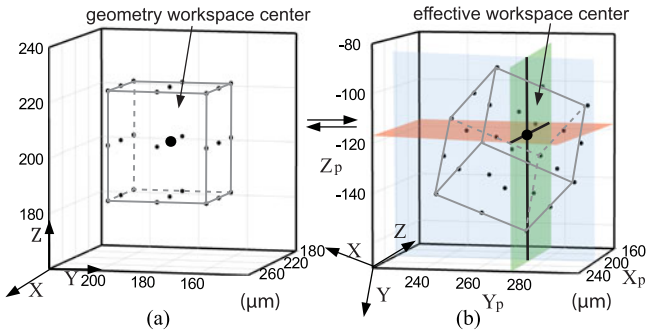

Fig. 5. (a) Geometry workspace center under image coordinates. (b) Effective workspace center determination under pole coordinates. The balanced planes in the X_p-direction, the Y_p-direction, and the Z_p-direction are shown in blue, green, and red, respectively.

is not the geometric center of the workspace. Because of the minute difference in the pole tips' shape, the coefficient k_i is different among three directions. To quantify magnetic force, the effective workspace center, the coefficient k_i for each direction, and the distance l need to be calibrated.

1) Determination of Effective Workspace Center: In effective workspace center calibration, we recorded the driving currents when the microbead was held in place at each of the 27 target positions set within a 40 μm $\times$ 40 μm $\times$ 40 μm cube selected around the geometric center of the workspace [see Fig. 5(a)]. As force balancing was reached when the bead was maintained in each position, magnetic force $\boldsymbol{F}$ was close to zero. According to (9), the center force $\boldsymbol{F_c}$, which is calculated by substituting the recorded driving current values into (7), is then linearly related to the bead position $\boldsymbol{P}$. In the effective workspace center where bead position $\boldsymbol{P}$ equals zero, the center force $\boldsymbol{F_c}$ should be zero. To clearly show force balancing in each direction, we used a magnetic

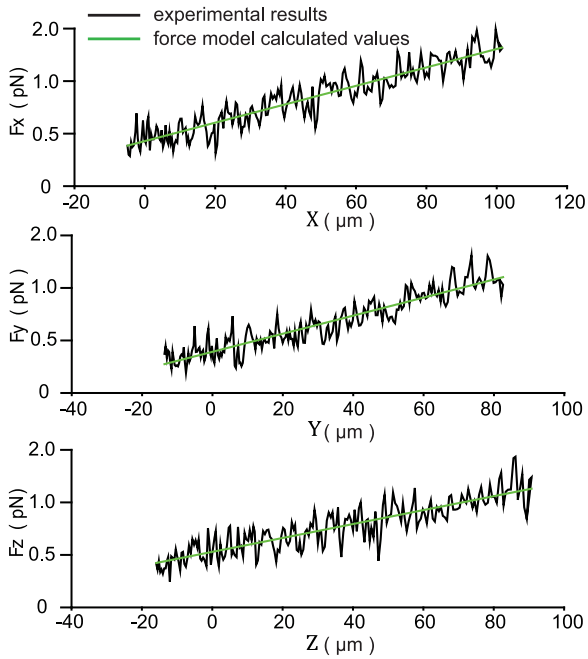

Fig. 6. Magnetic force determination. Constant currents of 0.5, 0.5, −0.1, −0.1, 0.1, and −0.9 A were applied to each coil to accelerate the bead. Black lines shows the force calculated from the bead dynamics using the viscosity value of 5 cps (10). Green line shows the model calculated force based on (9).

TABLE IV
CALIBRATION RESULTS

viscosity (cps)	k_{ix} ($\times 10^{-12}$)	k_{iy} ($\times 10^{-12}$)	k_{iz} ($\times 10^{-12}$)	l (μm)
1	3.50	3.70	3.91	496
5	3.52	3.70	3.70	495
10	3.39	3.98	4.00	503

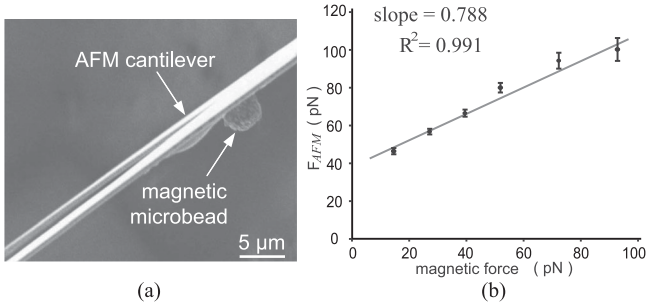

Fig. 7. (a) SEM image showing a magnetic microbead fixed on the back of an AFM cantilever for force calibration. (b) Experimentally measured AFM forces versus static magnetic forces determined by the force model (9). The slope and the coefficient of determination R^2 are also shown.

pole coordinate system, where all magnetic poles are located on the axes. The pole coordinate system is formed by using the direction from Pole 2 to Pole 4 as X_p, Pole 1 to Pole 3 as Y_p, and Pole 5 to Pole 6 as Z_p with pole numbering labeled in Fig. 2(c). The 27 target positions in the pole coordinate system are shown in Fig. 5(b). The force in each pole direction changes linearly with position, and the balanced position between each pair of poles was found in each direction, shown as the three balanced planes in Fig. 5(b). The intersection of the three planes was the calibrated effective workspace center.

2) Magnetic Force Determination: Quantifying the generated magnetic force is necessary for performing mechanical characterization. The microbead was accelerated within distilled water (viscosity: 1 cps at 20 °C) and silicone oils with known viscosities (5 cps, 10 cps, Brookfield). This range of viscosities was chosen to well cover the range of the viscosity of cells cytoplasm (2–3 cps) [25]. The magnetic forces were first determined with experimentally measured drag force and speed changes in silicone oil (5 cps) according to (11). The results are shown in Fig. 6, where the fluctuations in data were caused by thermal disturbances. According to the root-mean-square calculation, magnetic force resolution was determined to be better than 1.72 pN.

Furthermore, magnetic forces were also calculated by fitting driving current and bead positions into the force model (9) (see the green line in Fig. 6). The experimentally determined forces and theoretical values correlate well with the coefficient of determination R^2 of 0.867, 0.856, and 0.812 along the three directions. The fitted data (green line in Fig. 6) were used to calculate the coefficient k_i and the distance l in the three types of liquid with different viscosities. The results are summarized in Table IV.

Additionally, magnetic forces were further calibrated by gluing a magnetic microbead on an AFM cantilever [see Fig. 7(a)]. Thermal spectroscopy (Nanoscope 8.10) was performed to accurately measure the spring constant of the AFM cantilever (Spring constant 0.01 N/m, MSNL-10-C, Bruker) with the microbead fixed on its back. Applying currents to the coils exerted magnetic forces on the microbead and deformed the AFM cantilever. F_{AFM} was quantified with cantilever deformations and its spring constant. The model calculated force was obtained by using the average value of k_i and l, shown in Table IV and (9). Fig. 7(b) shows the calibration results. The deviations between forces measured by the AFM cantilever and the model calculated force reveal that magnetic force resolution is better than 3.75 pN.

B. Measurement of Intraembryonic Viscosity

The 3-D magnetic tweezer system was first applied to measure the cytoplasm viscosity. Mouse embryos were gathered 3.5 days past conception (early blastocyst stage) from the Canadian Mouse Mutant Repository in the Toronto Centre for Phenogenomics (TCP; Toronto, ON, Canada). The embryos were cultured with KSOM medium (EMD Millipore, Billerica, MA, USA) in a 35-mm petri dish and covered with mineral oil to prevent evaporation. The heating plate maintained the embryos at 37 ± 0.2 °C throughout the experiments.

Each embryo was transferred to the workspace chamber of the 3-D magnetic tweezer. A single magnetic microbead was microinjected with an injection micropipette (inner diameter: 5 μm) into the blastocyst embryo's cytoplasm. The microbead was then levitated and maintained in the focal plane, compensating the gravity and buoyancy of the bead. Then, exerting a force onto the bead in the XY plane resulted in the acceleration of the bead in the cytoplasm (supplementary video). The bead positions were recorded and the magnetic forces on the bead at different positions were quantified by the force model, (9). The viscosity of the cytoplasm was determined by fitting the bead velocity and force into (10) [see Fig. 8(c)].

The intraembryonic viscosity for early-stage blastocyst was measured to be 6.06±2.1 mPa·s (n=5), about eight times of the viscosity of water (about 0.7 mPa·s in 37 °C). In these embryos, the trophoblast cells contain sodium (Na^+) pumps, Na^+/K^+ ATPase and Na^+/H^+ exchangers, which pump sodium into the blastocyst cavity [26]. The

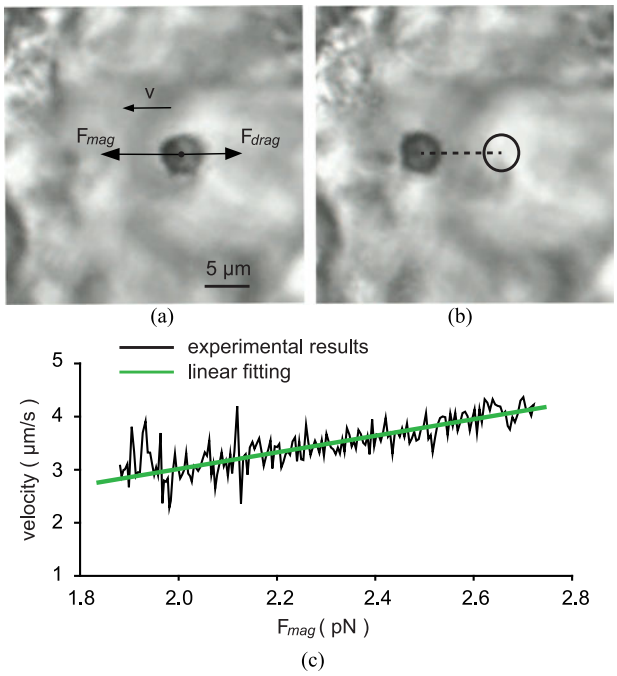

Fig. 8. Intraembryonic viscosity measurement. (a) and (b) Bead was levitated along the Z-axis and controlled to navigate in the XY plane. Bead positions, forces, and time were recorded simultaneously. (c) Intraembryonic cytoplasm viscosity was determined by fitting speed and force data into (10).

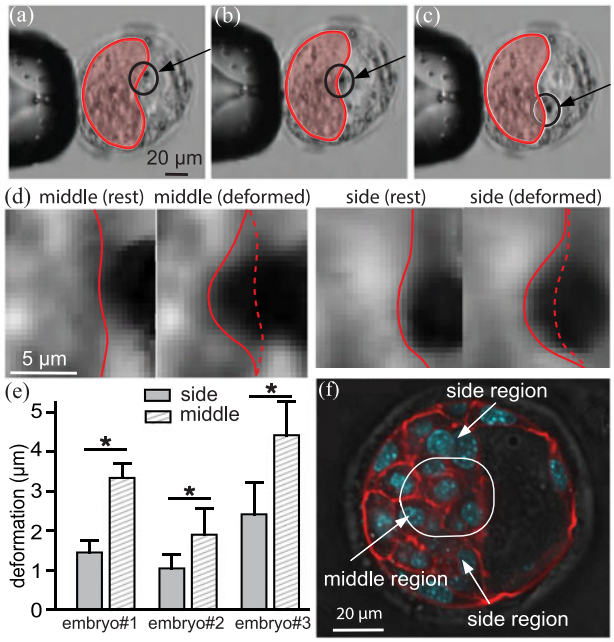

Fig. 9. Intraembryonic measurement at different locations on the ICM: (a) and (c) side regions, (b) middle region. ICM is marked in red. (d) Magnetic microbead deforms the ICM. (e) Deformations produced in the side and middle regions of the ICM in three embryos when a 60-pN force was applied by the microbead ($n = 5$ measurements). Error bar: standard deviations. $P<0.05$. Deformations were measured offline. (f) Confocal imaging shows actin and nucleus staining.

high concentration of sodium potentially results in a high viscosity of the cytoplasm in early-stage blastocysts [27].

C. Intraembryonic Mechanical Measurement

The 3-D magnetic tweezer system was applied to perform intraembryonic mechanical characterization. Since the force exerted by the microbead onto the ICM inside an embryo was nearly static, the static magnetic force calibration results [see Fig. 7(b)] were used for quantifying forces applied to cell structures. In addition, the subtle difference in intraembryonic pressure and ambient pressure has no impact in magnetic force application or quantification.

Similar to the viscosity measurement, the injected microbead in the blastocyst cavity was levitated to the focal plane, controlled to navigate inside the embryo toward different locations on the ICM [see Fig. 9(a)–(c)]. Then, the bead was controlled to apply forces in the normal direction to the ICM (see supplementary video). The resulting deformation was measured via microscopy imaging with a subpixel accuracy of 0.2 μm [see Fig. 9(d)] using Gaussian convolution [10]. When the magnetic microbead applied a force of 60 pN to the middle and side regions of the ICM, a deformation of 3.34±0.37 μm (n=5 measurements inside the same embryo) was produced in the middle region while the same force produced a deformation of 1.45±0.31 μm (n=5 measurements) in the side regions [embryo #1 in Fig. 9(e)]. Fig. 9(e) shows that under 60 pN, all the measured embryos revealed significantly larger deformations in the middle region than in side regions.

Taking advantage of the systems capability of applying accurate forces, mechanical characterization quantitatively revealed that the middle region of the ICM is more deformable than the side regions [see Fig. 9(e)]. By staining the cell nuclei and actin [see Fig. 9(f)], we measured the average cell number within a volume of 20 μm × 20 μm × 20 μm in the side regions to be seven cells versus 4.8 cells in the middle region. The average diameter of nuclei in the side regions was measured to be 9.4 μm versus 7.3 μm in the middle. The higher deformability of the middle region can be attributed to the lower cell density and smaller nuclei size. Higher cell density leads to denser cell compaction, and cell nuclei are known to be the stiffest organelle in a cell with a stiffness 5–10 times higher than cytoplasm [28]. These two factors together could lead to a higher stiffness in the side regions of the ICM, which was proven experimentally from the measurements made by our 3-D magnetic tweezer system.

V. Conclusion

This paper presented a 3-D magnetic tweezer system capable of navigating a microbead three dimensionally and performing mechanical measurements inside mouse embryos. Magnetic force was modeled and calibrated using fluids of known viscosities and AFM cantilevers. The system generates a high gradient field at the sharp pole tips and is capable of producing magnetic forces up to 120 pN with a resolution better than 4 pN. The cytoplasm viscosity was measured when navigating the bead with known forces inside the embryo, and the system was used to apply tens of picoNewton forces to multiple locations on the ICM of individual mouse embryos. The results indicate that the cytoplasm of blastocyst is about eight times of the viscosity of water, and the middle region of the ICM has a significantly lower stiffness than the side regions.

References

[1] L. Adamo *et al.*, "Biomechanical forces promote embryonic haematopoiesis," *Nature*, vol. 459, no. 7250, pp. 1131–1135, 2009.

[2] P. Krupinski, V. Chickarmane, and C. Peterson, "Simulating the mammalian blastocyst-molecular and mechanical interactions pattern the embryo," *PLoS Comput. Biol.*, vol. 7, no. 5, 2011, Art. no. e1001128.
[3] S. Wennekamp *et al.*, "A self-organization framework for symmetry breaking in the mammalian embryo," *Nature Rev. Mol. Cell Biol.*, vol. 14, no. 7, pp. 452–459, 2013.
[4] L. Z. Yanez *et al.*, "Human oocyte developmental potential is predicted by mechanical properties within hours after fertilization," *Nature Commun.*, vol. 7, 2016, art. no. 10809.
[5] K. Cockburn and J. Rossant, "Making the blastocyst: Lessons from the mouse," *J. Clin. Invest.*, vol. 120, no. 4, pp. 995–1003, 2010.
[6] M. Behrndt *et al.*, "Forces driving epithelial spreading in zebrafish gastrulation," *Sci.*, vol. 338, no. 6104, pp. 257–260, 2012.
[7] J. Liu, J. Wen, Z. Zhang, H. Liu, and Y. Sun, "Voyage inside the cell: Microsystems and nanoengineering for intracellular measurement and manipulation," *Microsyst. Nanoeng.*, vol. 1, 2015, p. 15020.
[8] H. Liu *et al.*, "Biophysical characterization of bladder cancer cells with different metastatic potential," *Cell Biochem. Biophys.*, vol. 68, no. 2, pp. 241–246, 2014.
[9] E. Shojaei-Baghini, Y. Zheng, and Y. Sun, "Automated micropipette aspiration of single cells," *Ann. Biomed. Eng.*, vol. 41, no. 6, pp. 1208–1216, 2013.
[10] J. Liu *et al.*, "Robotic fluidic jet for automated cellular and intracellular mechanical characterization," in *Proc. IEEE Int. Conf. Inf. Autom.*, 2016, pp. 462–467.
[11] H. Zhang and K.-K. Liu, "Optical tweezers for single cells," *J. Roy. Soc. Interface*, vol. 5, no. 24, pp. 671–690, 2008.
[12] E. Diller and M. Sitti, "Untethered magnetic micromanipulation," in *Micro-and Nanomanipulation Tools*, vol. 13, Hoboken, NJ, USA: Wiley, 2015.
[13] K. E. Peyer, L. Zhang, and B. J. Nelson, "Bio-inspired magnetic swimming microrobots for biomedical applications," *Nanoscale*, vol. 5, no. 4, pp. 1259–1272, 2013.
[14] S. Tottori *et al.*, "Magnetic helical micromachines: Fabrication, controlled swimming, and cargo transport," *Adv. Mater.*, vol. 24, no. 6, pp. 811–816, 2012.
[15] L. Zhang *et al.*, "Characterizing the swimming properties of artificial bacterial flagella," *Nano Lett.*, vol. 9, no. 10, pp. 3663–3667, 2009.
[16] I. S. M. Khalil, V. Magdanz, S. Sanchez, O. G. Schmidt, and S. Misra, "Precise localization and control of catalytic Janus micromotors using weak magnetic fields," *Int. J. Adv. Robot. Syst.*, vol. 12, pp. 1–7, 2015.
[17] S. Schuerle, S. Erni, M. Flink, B. E. Kratochvil, and B. J. Nelson, "Three-dimensional magnetic manipulation of micro- and nanostructures for applications in life sciences," *IEEE Trans. Magn.*, vol. 49, no. 1, pp. 321–330, Jan. 2013.
[18] P. Ryan and E. Diller, "Five-degree-of-freedom magnetic control of microrobots using rotating permanent magnets," in *Proc. IEEE Int. Conf. Intell. Robots Syst.*, 2016, pp. 1731–1736.
[19] M. Vonthron, V. Lalande, G. Bringout, C. Tremblay, and S. Martel, "A MRI-based integrated platform for the navigation of microdevices and microrobots," in *Proc. IEEE Int. Conf. Intell. Robots Syst.*, 2011, pp. 1285–1290.
[20] A. R. Bausch, W. Möller, and E. Sackmann, "Measurement of local viscoelasticity and forces in living cells by magnetic tweezers," *Biophys. J.*, vol. 76, no. 1, 1999, pp. 573–579.
[21] C. Guilluy *et al.*, "Isolated nuclei adapt to force and reveal a mechanotransduction pathway in the nucleus," *Nature Cell Biol.*, vol. 16, no. 4, pp. 376–381, 2014.
[22] Z. Zhang and C. H. Menq, "Trapping and steering a magnetic microbead using 3D magnetic tweezers," *Proc. ASME Dyn. Syst. Control Conf.*, 2010, pp. 1–5.
[23] D. Matsuura, H. Aoki, and Y. Takeda, "Development of a 3D-magnetic tweezer system having magnetic pole positioning mechanism," in *Proc. IEEE Int. Conf. Intell. Robots Syst.*, 2016, pp. 1745–1750.
[24] Z. Zhang, K. Huang, and C. H. Menq, "Design, implementation, and force modeling of quadrupole magnetic tweezers," *IEEE/ASME Trans. Mechatronics*, vol. 15, no. 5, pp. 704–713, Oct. 2010.
[25] A. M. Mastro *et al.*, "Diffusion of a small molecule in the cytoplasm of mammalian cells," *Proc. Nat. Acad. Sci. USA*, vol. 81, no. 11, pp. 3414–3418, 1984.
[26] J. M. Baltz, S. S. Smith, J. D. Biggers, and C. Lechene, "Intracellular ion concentrations and their maintenance by Na+/K(+)-ATPase in preimplantation mouse embryos," *Zygote*, vol. 5, no. 01, pp. 1–9, 1997.
[27] F. M. Manejwala, E. J. Cragoe, and R. M. Schultz, "Blastocoel expansion in the preimplantation mouse embryo: Role of extracellular sodium and chloride and possible apical routes of their entry," *Develop. Biol.*, vol. 133, no. 1, pp. 210–220, 1989.
[28] H. Liu *et al.*, "In situ mechanical characterization of the cell nucleus by atomic force microscopy," *ACS Nano*, no. 4, pp. 3821–3828, 2014.